



Evaluation of phase and domain switching in Sn-doped BCZT piezoceramics with coexisting ferroelectric phases

Abhijit Pramanick^{a,b,c,*}, Laurent Daniel^{b,c,**}, Sarangi Venkateshwarlu^a, Valentin Segouin^{b,c}, Yang Ren^{a,d}

^a Department of Materials Science and Engineering, City University of Hong Kong, Kowloon, Hong Kong Special Administrative Region

^b Université Paris-Saclay, CentraleSupélec, CNRS, Laboratoire de Génie Electrique et Electronique de Paris, 91192 Gif-sur-Yvette, France

^c Sorbonne Université, CNRS, Laboratoire de Génie Electrique et Electronique de Paris, 75252 Paris, France

^d Advanced Photon Source, Argonne National Laboratory, Argonne, IL, United States

ARTICLE INFO

Keywords:

Piezoelectric
Ferroelectric
Phase transition
X-ray diffraction
Micromechanical modeling

ABSTRACT

Large electrostrain properties are often observed in piezoelectric ceramics for conditions favoring a coexistence of multiple ferroelectric phases. However, the prevalence of different electric-field-induced microscopic mechanisms, viz. phase transition and domain switching, and their relative roles towards macroscopic electrostrain response are not readily understood. Here, we used *in situ* synchrotron X-ray diffraction and micromechanical modeling to self-consistently describe the electric-field-induced microscopic mechanisms in grains of different orientations in a polycrystalline Pb-free piezoceramic. We reveal, from experimental and modeling results, a unique tetragonal-to-orthorhombic-to-tetragonal phase transformation induced under low electric fields (< 1 kV/mm) in grains with 002 crystallographic poles oriented either within 20° or orthogonal to the applied electric-field direction. In contrast, grains with their 002 poles oriented 30°–80° to the electric-field direction undergo a continuous tetragonal-to-orthorhombic transformation for electric fields larger than 1 kV/mm. These results emphasize the critical role of a phase-transition-assisted domain switching mechanism in grains of specific orientations towards realizing a large electrostrain coefficient of $d_{33} \sim 600$ pm/V under low electric fields (< 1 kV/mm) in the Pb-free Sn-doped (Ba,Ca)(Zr,Ti)O₃ piezoceramic.

1. Introduction

Piezoelectric ceramics (or piezoceramics, in short) exhibit high degree of electromechanical coupling in the solid state, that is, they exhibit large polarization changes in response to mechanical stress and conversely exhibit large strains in response to applied electric fields [1]. Consequently, they are of vital significance in many different areas of applications, including load sensors, precision actuators, telecommunications, energy harvesting, and biomedical imaging [2–6]. For application of piezoceramics as precision actuators, some of the desirable characteristics include their large electric-field-induced strains, low energy consumption, stability with respect to electric-field amplitude and temperature, and good fatigue endurance [2], [7–9]. These characteristics can be engineered in piezoceramics by controlling the microscopic mechanisms underlying their macroscopic electromechanical strains, viz. lattice strains, ferroelectric/ferroelastic domain switching,

phase transition etc [10–13]. Traditionally, the industrial and commercial piezoceramics have overwhelmingly been comprised of lead (Pb)-based materials, most notably the lead zirconate titanate or PZT [1]. However, recent environmental concerns regarding the synthesis and disposal of Pb-based piezoceramics have intensely driven research on Pb-free piezoceramics over the last decade [14]. While several potential candidates to replace PZT have been developed, engineering of material properties over a broader set of performance metrics, such as strain, energy consumption or stability, has proved to be elusive [15,16]. One underlying challenge in this regard is to elucidate the several microscopic mechanisms that may be triggered under the application of electric fields and their relative contributions to the macroscopic electromechanical strain [17–21]. For many of the recently developed Pb-free piezoceramics, high electromechanical strains are observed for composition or temperature ranges which allow for a coexistence of several crystallographic phases [22–26]. The large electromechanical

* Corresponding author at: Department of Materials Science and Engineering, City University of Hong Kong, Kowloon, Hong Kong Special Administrative Region.

** Corresponding author at: Université Paris-Saclay, CentraleSupélec, CNRS, Laboratoire de Génie Electrique et Electronique de Paris, 91192 Gif-sur-Yvette, France.

E-mail addresses: apramani@cityu.edu.hk (A. Pramanick), laurent.daniel@centralesupelec.fr (L. Daniel).

<https://doi.org/10.1016/j.jeurceramsoc.2023.01.051>

Received 21 November 2022; Received in revised form 18 January 2023; Accepted 25 January 2023

Available online 26 January 2023

0955-2219/© 2023 The Author(s). Published by Elsevier Ltd. This is an open access article under the CC BY-NC-ND license (<http://creativecommons.org/licenses/by-nc-nd/4.0/>).

strains in these materials have been associated with the triggering of an electric-field-induced phase transition, which may be concurrent with other microscopic mechanisms such as lattice strains or domain switching [22–31]. Nevertheless, it is challenging to characterize quantitatively the degree of electric-field-induced phase transition in the case of a confluence of multiple microscopic strain mechanisms.

In situ X-ray diffraction is a broadly accepted non-destructive experimental technique for the characterization of microscopic mechanisms in the bulk volume of piezoceramics materials [18–21]. The microscopic structural changes induced under external stimulus can be characterized from the observed changes in the position and shape of the diffraction peaks. In general, two different approaches can be undertaken. One approach involves least-square fitting of the diffraction pattern over several *hkl* peaks using the Rietveld refinement method [32], in order to determine the changes in phase and domain variant fractions [33–35]. This, however, has two limitations. First, one has to consider that the different *hkl* peaks originate from crystallites that are differently oriented with respect to an external stimulus, such as electric field, and therefore they may not undergo similar structural phase transition. Secondly, although one can potentially address the issue of anisotropic strains in the crystallites by incorporating certain presumed orientation distribution function [36], such a function may itself be a function of electric-field magnitude and therefore can have an unpredictable influence on the Rietveld refinement results. Indeed, earlier work has shown that a full pattern Rietveld refinement approach may yield misleading conclusions for domain texture in case of concurrent phase and domain switching in piezoceramics [35]. In an alternative approach, one can characterize the structural changes for a certain family of similarly oriented crystallites by fitting individual *hkl* diffraction peaks for different azimuthal orientations [18–21], [37]. This second approach has been widely applied for quantitative evaluation of induced structural changes, viz. lattice strains and domain switching, and for calculating their respective contributions to the macroscopic electromechanical strains in piezoceramics [18–21]. However, electric-field-induced changes in phase fractions are not discussed often. While some diffraction studies have provided limited insights into the effect of grain orientations on electric-field-induced phase transitions in piezoceramics [35,38], the origin of such behavior is not yet clear. Here, we have addressed this issue for the Pb-free Sn-doped (Ba,Ca)(Zr,Ti)O₃ (BCZT) piezoceramics.

Recently, we reported exemplary performance of Sn-doped BCZT piezoceramics with composition close to the orthorhombic-tetragonal phase boundary, with regard to their large electromechanical strain (~0.2% at room temperature), large piezoelectric coefficient of $d_{33}^* = 800$ pm/V for electric field below 1 kV/mm, minimal hysteresis and thermal stability comparable to commercial PZT ceramics [31]. The addition of Sn by a small amount (~1 at%) was shown to sustain higher values of d_{33}^* from room temperature to 140 °C as compared to undoped BCZT compositions, such as shown in Fig. 9 in ref. [31]. Based on *in situ* X-ray diffraction experiments, we qualitatively determined that the large electromechanical strains in Sn-doped BCZT are underpinned by a unique microscopic mechanism, whereby polarization switching is aided by a reversible tetragonal-orthorhombic phase transition. Intriguingly, the *in situ* diffraction results suggest that one domain variant of the initial tetragonal phase transitions to an orthorhombic phase for intermediate values of electric-field amplitudes, before switching back to a second variant of the tetragonal phase. In this work, we have expanded on our earlier finding to clarify how such a phase transition mechanism depends on the orientation of the microscopic grains. This is made possible by detailed characterization of *in situ* diffraction patterns from all orientation space and improved peak fitting method. Furthermore, the relative extent of concurrent phase and domain switching processes are validated using a micromechanical modeling approach. Our work provides clarity regarding the significance of electric-field-induced phase transition towards large strains in

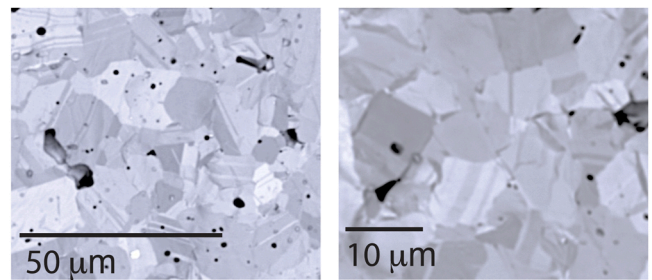


Fig. 1. SEM images of the fracture surface of a ceramic sample. The observable subgrain features correspond to domains and domain boundaries.

polycrystalline ceramics, which will be broadly applicable to many piezoceramic materials.

2. Experimental

2.1. Materials

Piezoelectric ceramics of nominal composition (Ba_{0.95}Ca_{0.045}Sn_{0.005})(Ti_{0.875}Zr_{0.12}Sn_{0.005})O₃, or Sn-doped BCZT, were used in this study. The details regarding the synthesis procedure were described in the ref. [31]. In short, precursor oxides were mixed by ball-milling and subsequently calcined at a temperature of 1350 °C. The calcined powder was then ball-milled, mixed with organic binder, pressed into pellets and sintered at a temperature of 1450 °C. The sintered ceramics were then first annealed under reducing condition at 1100 °C, and subsequently annealed in air, which aided the incorporation of Sn into A/B sites while minimizing electronic defects. In addition, a prolonged heat treatment lower temperature can also promote finer grain structure [39]. Finally, the sintered pellets were polished, electroded, and used for electromechanical characterization. For detailed structural information on the synthesized materials, please see ref. [31].

The grain size was characterized from Scanning Electron Microscope (SEM) image of the cross-section of a ceramic pellet. A Thermo Scientific™ XL G2 Desktop Scanning Electron Microscope (SEM) was used for this purpose. Fig. 1 shows representative images of the fracture surface of a ceramic sample. Based on these images, the grain size is estimated to be between 5 and 15 μm. The subgrain features correspond to the domains and domain boundaries within each grain. The average crystallite size for the present ceramics was also estimated based on Scherrer equation, $d_{\text{crystallite}} \sim 2\pi/\Delta q$, where Δq is the width of the diffraction peak in terms of wavevector q . For this estimation, widths of 002 and 200 peaks were considered (shown below), which were fit with Pearson VII peak profile function (vide infra). Based on the measured diffraction peak width, the average crystallite (domain) size is estimated to be ~0.2 μm, which would correspond to grains of a few micrometers. This is consistent with the SEM images shown in Fig. 1. The grain size observed here for Sn-doped BCZT ceramics is slightly lower than those reported for BCZT ceramics synthesized using conventional sintering such as ref. [12], but is similar to those reported in ref. [39] for a two-step sintering procedure.

2.2. Electromechanical measurements

The electric-field-induced strain response of the Sn-doped BCZT ceramics was measured using Digital Image Correlation (DIC). The detailed description of the experimental setup and data analysis was provided in earlier references [31,40–45]. In short, DIC is a non-contact optical technique that can measure full-field displacements at the surface of a sample [40–43]. Applied to ferroelectrics, it can provide access to electric-induced strains down to 3×10^{-6} (standard deviation on the average value) and permits determining piezo-electric coefficients of the order of 20 pm/V and above [40–44]. Furthermore, a previous study

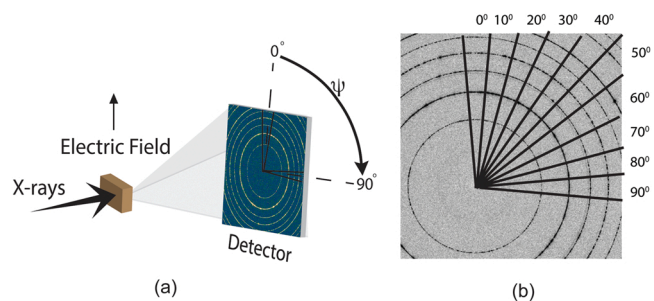


Fig. 2. (a) Experimental set-up for *in situ* X-ray diffraction under applied electric fields. Ψ refers to the azimuthal angle with respect to the electric field direction. (b) Image of the 2-dimensional diffraction pattern showing the definition of the different azimuthal sectors.

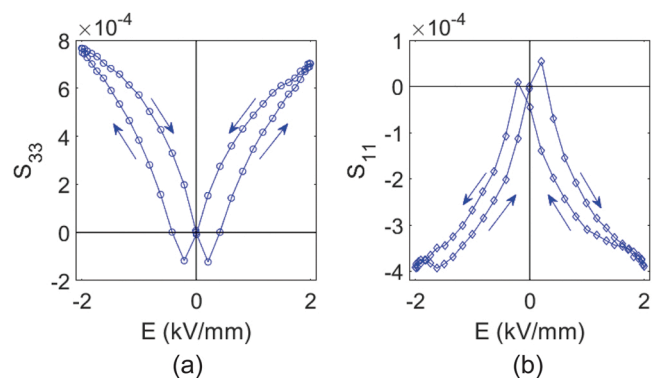


Fig. 3. DIC results: (a) longitudinal, S_{33} , and (b) transverse, S_{11} , strain components.

showed that DIC-based strain field measurements can help to distinguish the contribution of isochoric mechanisms (i.e., domain switching) from non-isochoric mechanisms (e.g., piezoelectricity or crystal phase transition) [31]. In the current study, DIC spectroscopic measurements were undertaken, while the sample was subjected to a sinusoidal electric field of frequency 80 mHz and amplitude 2000 V/mm [31].

2.3. *In situ* diffraction measurements

The *in situ* X-ray diffraction experiment under applied electric field was undertaken at the Sector 11-ID of the Advanced Photon Source (APS) at the Argonne National Laboratory. The experimental set-up is shown in Fig. 2. Further details for *in situ* experiments are provided in ref. [31]. Specifically, the wavelength of the high-energy X-rays used for the experiment was 0.1173 Å and the diffraction measurements were taken using a 2-dimensional detector in the transmission mode. A 1 mm × 1 mm × 5 mm ceramic sample was used for *in situ* X-ray measurements, while the electric-field was applied across the 1 mm × 1 mm face. The X-ray beam dimensions were 100 μm × 100 μm. Initially, the sample was poled under an applied electric field of 2000 V/mm. Then, 2-dimensional diffraction images were obtained under step-wise incremental electric-field amplitudes. The measured 2-dimensional diffraction image for each electric-field amplitude was segmented into different azimuthal sectors, such as shown in Fig. 2. 1-dimensional diffraction patterns were then obtained for different azimuthal sectors using the software Fit2D. The measured diffraction intensities were integrated over 10-degree windows in order to obtain good statistics for the corresponding 1-dimensional diffraction patterns, as presented below, and in the Fig. S1 in the Supplementary Information. For quantitative characterization of electric-field-induced structural changes in the material, the diffraction peaks were fit using Pearson VII peak profile function [19].

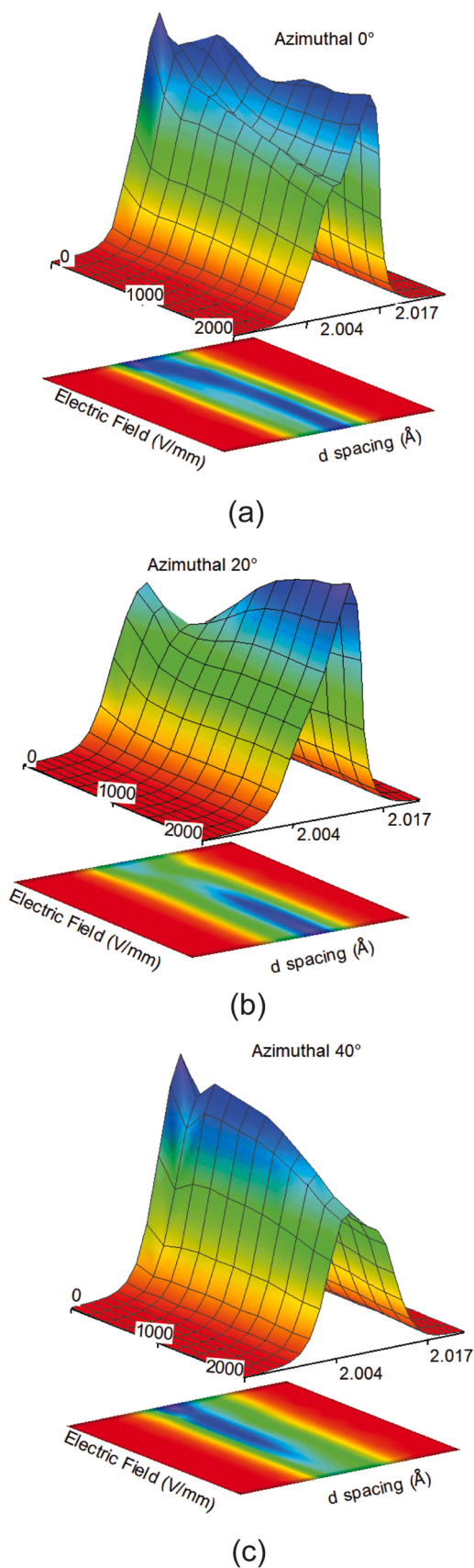


Fig. 4. Surface and contour plots of electric-field-induced changes for azimuthal angular sectors of (a) 0°, (b) 20°, and (c) 40°, with respect to the electric-field-direction.

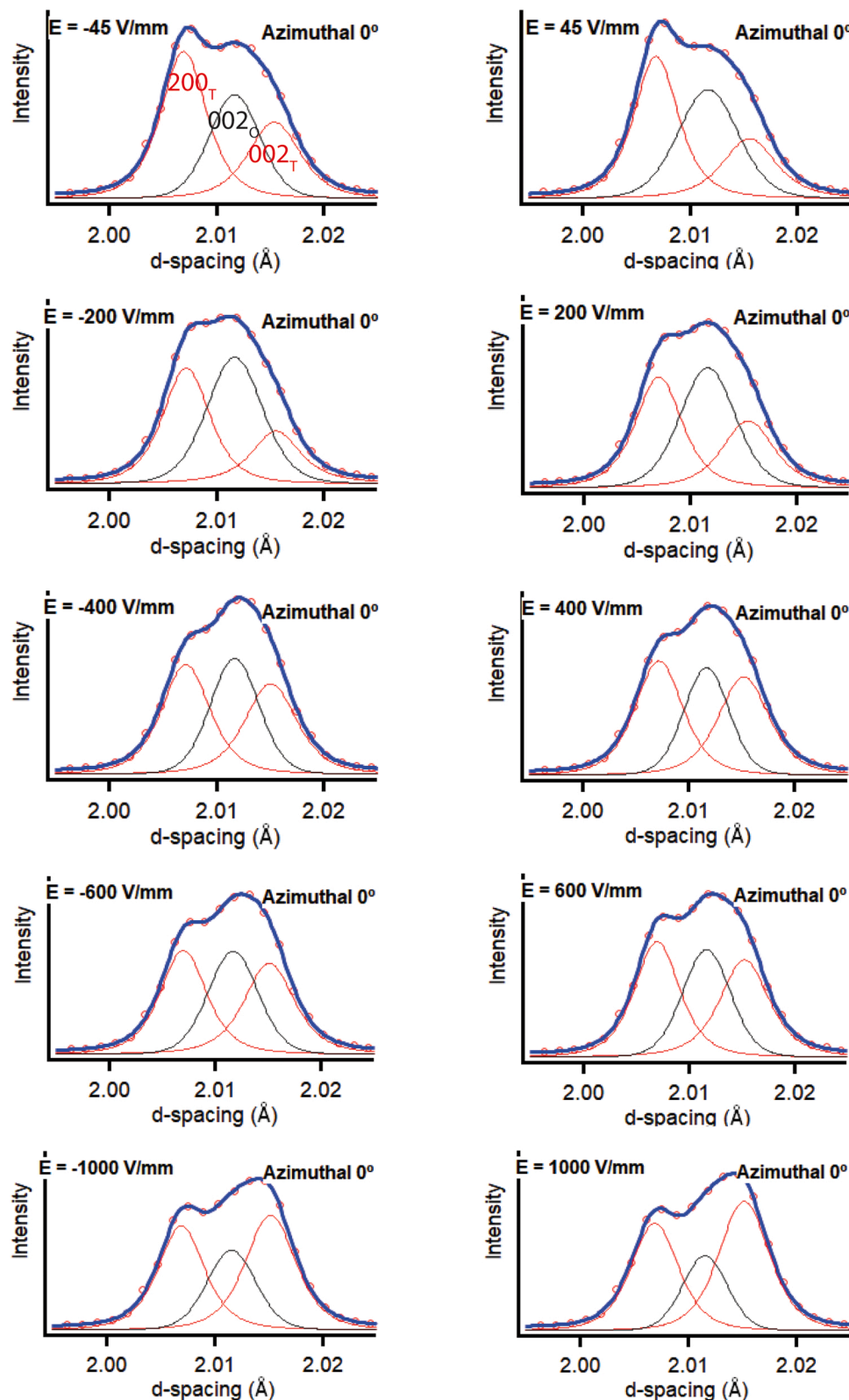


Fig. 5. 002_{pc} diffraction peak profiles for the azimuthal angle of 0° for different magnitudes of applied electric fields. The red peaks represent reflections from the tetragonal (T) 90° domain variants, while the black peak is from the orthonhombic (O) phase.

During the *in situ* experiments, the electric-field amplitude was first increased step-wise from -45 V/mm to a maximum negative field of -2000 V/mm and then brought back down to zero. The cycle was repeated for positive incremental electric-field-amplitudes for a maximum electric-field of 2000 V/mm.

3. Results

3.1. Macroscopic electric-field induced strains

Fig. 3 shows the electric-field-dependent normal strain (S_{33} , along

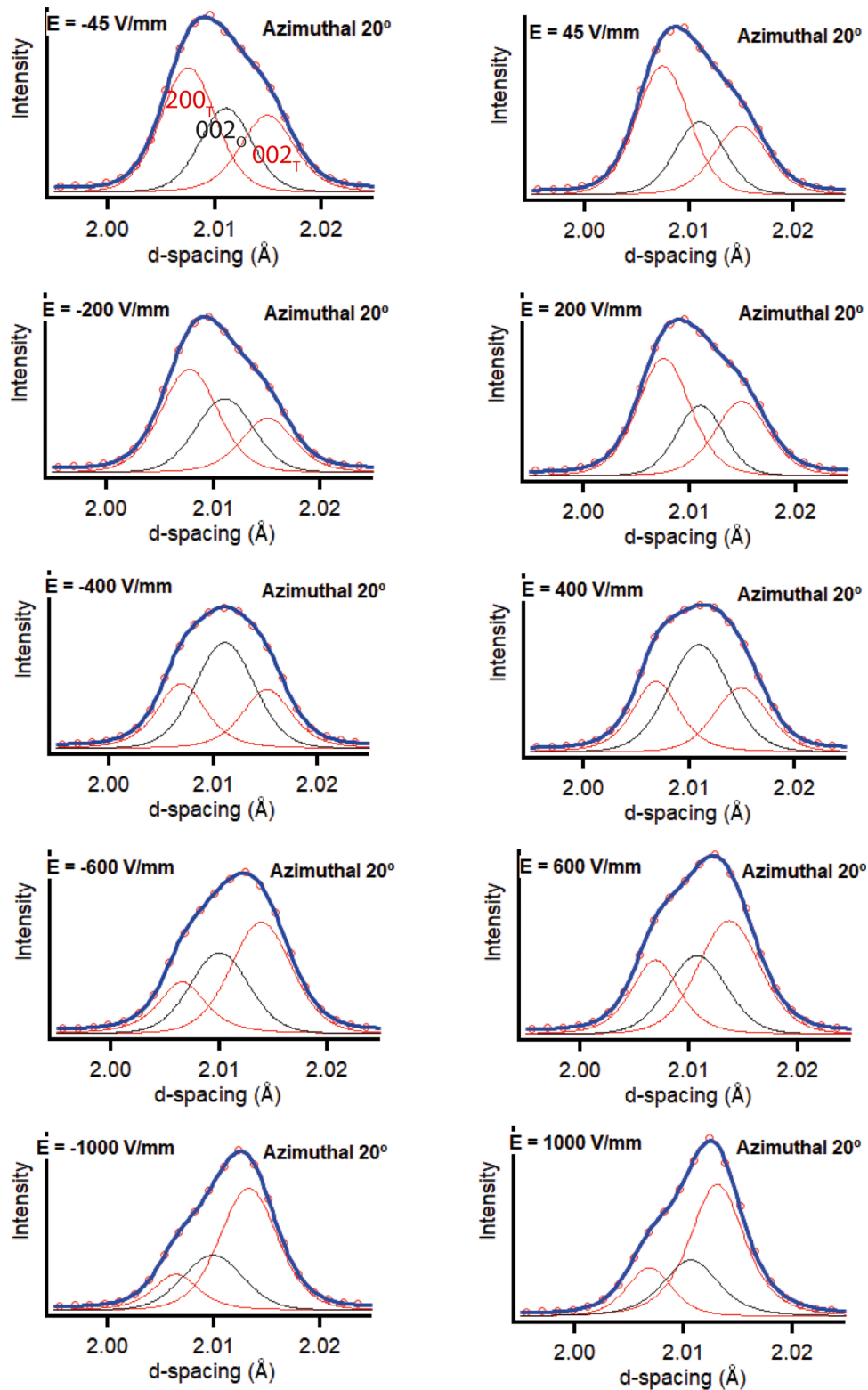


Fig. 6. 002_{pc} diffraction peak profiles for the azimuthal angle of 20° for different magnitudes of applied electric fields. The red peaks represent reflections from the tetragonal (T) 90° domain variants, while the black peak is from the orthorhombic (O) phase.

the field direction) and the transverse strain (S_{11} , perpendicular to the field direction) obtained from DIC measurements [31]. At 2 kV/mm, the mean strain (defined as $\Delta l/l$, where l represents the original dimension) values S_{33} and S_{11} are 7.7×10^{-4} and -4×10^{-4} , respectively. The corresponding values for electrostrain coefficients are $d_{33}^* \sim$

385 pm/V and $d_{31}^* \sim -195$ pm/V at 2 kV/mm. For electric-field of

1 kV/mm, the corresponding electrostrain coefficients are $d_{33}^* \sim 600$ pm/V and $d_{31}^* \sim -250$ pm/V. The absolute value of the shear component $|S_{31}|$ does not exceed 6% of the total S_{33} amplitude and is hence neglected. The trace of the strain tensor, assumed to be defined as $S_{33} + 2S_{11}$, defines the volume change of the material during the test. As shown in ref. [31], for Sn-doped BCZT, there is large deviation from zero

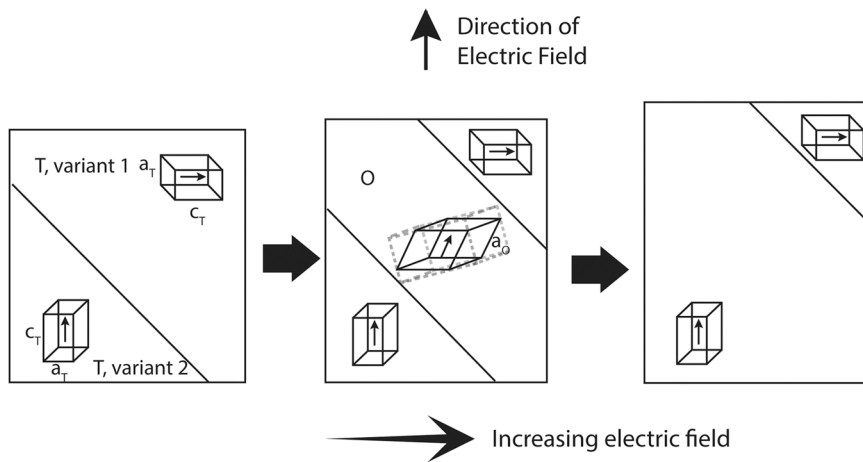


Fig. 7. Schematic illustration of the mechanisms for transformation from the T phase to the intermediate O phase, and subsequent change in the volume fraction of the 90° domain variants of the T phase. For the intermediate O phase, the dotted line indicates the conventional orthorhombic unit-cell, while the solid line indicates the equivalent “monoclinic” unit-cell [1]. a_T and c_T correspond to the dimensions of the tetragonal unit cell. a_O correspond to the dimension of the equivalent “monoclinic” unit-cell of the O phase.

for the factor $S_{33} + 2S_{11}$ for electric-fields < 1 kV/mm, which is indicative of non-conservation of the total material volume and therefore phase transition in the material over a wide electric-field range [31].

3.2. Quantitative characterization of microscopic mechanisms

Fig. 4 shows the contour and surface plots for 002_{pc} peak, as functions of electric-field amplitude during incremental negative electric-field steps for three different azimuthal sectors. Similar changes in peak profiles were observed for applied incremental positive electric fields. The subscript pc refers to the pseudocubic notation. Fig. 4(a) shows the changes in the 002_{pc} peak for the azimuthal sector 0° , that is, for grains that have their 002_{pc} crystallographic poles oriented parallel to the electric-field direction. Figs. 4(b) and 4(c) show the contour and surface plots for 002_{pc} peak as a function of electric-field amplitude during incremental negative electric-field steps for the azimuthal sectors 20° and 40° , respectively. Clearly, the observed peak profile changes are different for the grains that have their 002_{pc} poles either parallel to, or at an orientation, to the applied electric-field direction.

The corresponding 1-dimensional peak profiles for the 0° and 20° azimuthal sectors, and for both negative and positive electric fields, are shown in Figs. 5 and 6, respectively. At room temperature, there is a coexistence of tetragonal (T) and orthorhombic (O) phases in the material [31]. Therefore, the peak profiles measured at different electric-field amplitudes are best fit by three symmetric peaks, which correspond to the $(002/200)_T$ peaks of the T phase and $\{002\}_O$ peak of the O phase. The $\{002\}_O$ peaks are not separated due to smaller distortion of the unit cell of the O phase [31], as compared to the tetragonal unit cell. The positions of the $(002/200)_T$ peaks and the $\{002\}_O$ peaks are marked in Figs. 5,6. During fitting of the diffraction peaks, the following constraints are imposed: (a) the peak positions of the T and O phases are allowed to change within narrow constraints, which means that the $\{001\}$ planes of the phases did not strain significantly with the application of electric field so as to alter the T/O phase distinction, and (b) the relative peak widths for the T and O phases are maintained to be similar (not same) so as not to exceed the difference between the respective peak positions, such as refs.[19,46]. The first point is supported by insignificant electric-field induced strains for $002/200$ diffraction peaks in BCZT ceramics, such as ref. [47].

For the 0° azimuthal sector (Fig. 5), by comparing the peak profiles measured for applied electric fields of -45 V/mm and -1000 V/mm, we can observe an intensity interchange between the 200_T and 002_T peaks. This is indicative of 90° domain switching in the T phase. However, for intermediate electric field of 200 V/mm, we also observe an increase in the $\{002\}_O$ peak intensity, which indicates an increase in the volume fraction of the O phase. The intensity of the $\{002\}_O$ peak decreases with further increase in electric field to 1000 V/mm. For the 20°

azimuthal sector (Fig. 6), the electric-field-induced changes in the 002_{pc} peak profile for the 40° azimuthal angle, which are markedly different from what is observed in Figs. 5,6. For the 40° azimuthal angle, that is, for grains that have their 002_{pc} crystallographic poles oriented 40° with respect to the electric-field direction, we observe a continuous increase in the $\{002\}_O$ peak intensity, but no significant intensity interchange between the 002_T and 200_T peaks. This indicates that for these grain orientations, the primary electric-field-induced structural changes involve a continuous T -to- O phase transformation.

The above results importantly show that the electric-field-induced changes in the T/O phase fractions and domain variants in the T phase are both strong functions of the grain orientation. The method for quantitative depiction of phase and domain variant fractions is described below.

3.2.1. Changes in orthorhombic phase volume fraction F_O

The volume fraction of the orthorhombic O phase, F_O , is determined based on the following equation:

$$F_O = \frac{I[\{002\}_O]}{I[200_T] + I[002_T] + I[\{002\}_O]} \quad (1)$$

where I represents the integrated intensities of the respective peaks. Fig. 9 shows the electric-field-dependent changes in F_O for the various azimuthal angles with respect to the electric-field direction. Fig. 10 shows the electric-field-dependent changes in the two tetragonal domain variants, F_{200_T} (a -domains) and F_{002_T} (c -domains), for the various azimuthal angles, with respect to the electric-field direction, for positive and negative applied electric fields. For the azimuthal angles of $0^\circ - 20^\circ$, there is an initial increase in F_O with increasing electric field below 400 V/mm, which is followed by a subsequent decrease in F_O for higher electric fields. For the azimuthal angle of 30° , we observe minimal changes in F_O with increasing electric fields. In contrast, for the 40° azimuthal angle, a continuous increase in F_O is observed with increasing electric field, which becomes more prominent for electric fields higher than 800 V/mm. Similar field-dependence is observed for the azimuthal angles of $50^\circ - 80^\circ$, although the magnitude of change in F_O is different

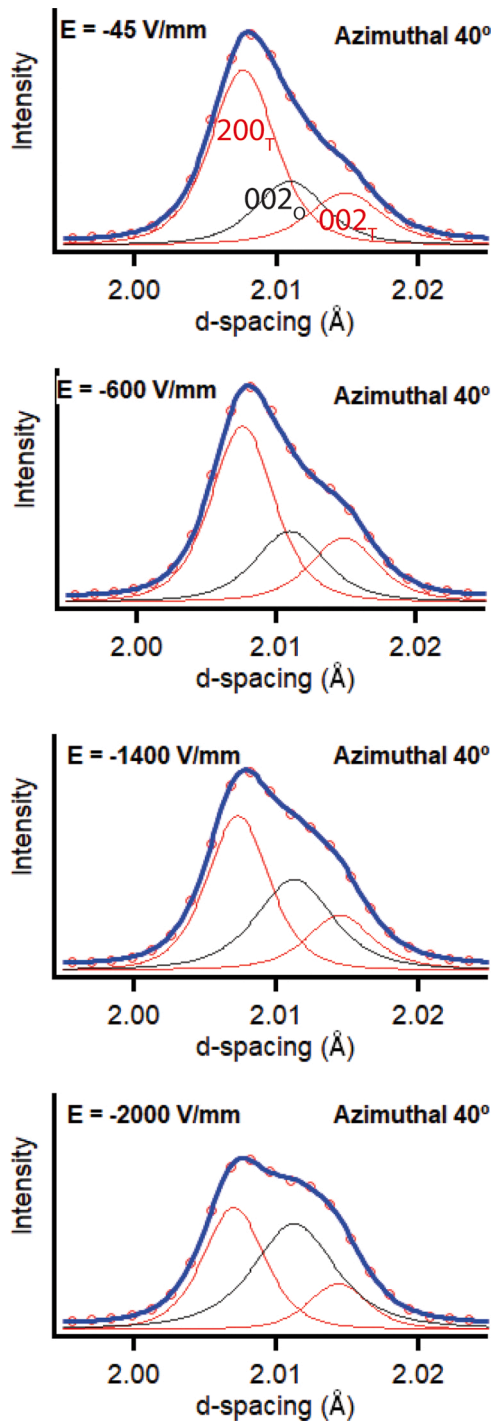


Fig. 8. 002_{pc} diffraction peak profiles for the azimuthal angle of 40° for different magnitudes of applied electric fields. The red peaks represent reflections from the tetragonal (T) 90° domain variants, while the black peak is from the orthorhombic (O) phase.

for the different angles. For azimuthal angle of 60°, there are minimal changes in T/O phase fractions. In addition, F_O increases at the expense of F_{200_T} variant for 40° azimuthal, while F_O increases at the expense of F_{002_T} variant for azimuthal angles of 50°–80°. Interestingly, for the azimuthal angle of 90°, F_O decreases for electric fields higher than 800 V/mm, while a corresponding increase (decrease) in F_{200_T} (F_{002_T}) is observed.

We note that the current results are consistent with those described by Guo et al. in ref. [29]. Using transmission electron microscopy (TEM),

Guo et al. showed that for ceramics of composition 0.5Ba(Zr_{0.2}Ti_{0.8})O₃–0.5(Ba_{0.7}Ca_{0.3})TiO₃: (a) the application of a moderate electric field of 200–300 V/mm transforms a multiphase, multivariant domain structure to a single variant structure of orthorhombic phase, and (b) further increase in electric field causes the transitional orthorhombic phase to transform back to a multidomain structure of a presumably tetragonal phase. Indeed, this is similar to what is observed in the current study, such as an initial increase in orthorhombic phase fraction, F_O , followed by an eventual decline in F_O under higher electric fields, for azimuthal sectors 0°–20°. Although the results presented by Guo et al. are qualitatively similar to the current results, it should be noted that the composition of the materials used in these two studies are slightly different. Nevertheless, the qualitative similarities between the results presented in ref. [29] and that of the current study indicates that the induction of a transitional orthorhombic phase under intermediate electric fields, followed by its transformation to a multidomain structure of tetragonal phase at higher electric fields, may be generally true for a broad range of BCZT compositions.

3.2.2. 90° domain switching in the tetragonal phase

Similarly, the respective volume fractions of the two tetragonal 90° domain variants are determined as follows:

$$F_{200_T} = \frac{I[200_T]}{I[200_T] + I[002_T] + I[\{002\}_O]} \quad (2)$$

$$F_{002_T} = \frac{I[002_T]}{I[200_T] + I[002_T] + I[\{002\}_O]} \quad (3)$$

Fig. 10 shows the electric-field-dependent changes in F_{200_T} and F_{002_T} for the various azimuthal angles with respect to the electric-field direction, for negative applied electric fields. Similar changes in the F_{200_T} and F_{002_T} for the various azimuthal angles were observed for positive applied electric fields (see Fig. S2 in the Supplementary Information). The relative volume fraction of the c domain at any given electric field is simply obtained as $\eta = F_{002_T} / (F_{002_T} + F_{200_T})$. The fractional switching between the 90° domain variants in the tetragonal phase is obtained as $\Delta\eta = \eta_{1000} - \eta_{45}$, where η_{1000} and η_{45} refer to the 90° domain volume fractions for electric-field magnitudes of 1000 V/mm and 45 V/mm, respectively. Fig. 11 shows $\Delta\eta$ as a function of azimuthal angle with respect to the electric-field direction. The orientation dependence of $\Delta\eta$ is similar to what has been generally observed for other ferroelectric materials, where the domain switching fraction changes from positive to negative with increasing angles with respect to the electric-field direction, with the crossover occurring close to 50° azimuthal angle. However, interestingly $\Delta\eta$ is significantly higher for the 20° azimuthal angle than all other orientations for electric fields lower than 1000 V/mm. With further increase in electric field above 1000 V/mm, the $\Delta\eta$ for the 20° azimuthal angle saturates, while the $\Delta\eta$ continues to increase for other azimuthal angles. The significantly larger $\Delta\eta$ for the 20° orientation can be correlated with a large electric-field-dependent change in F_O at lower electric fields (Fig. 9).

4. Micromechanical modeling

In order to provide a description of both domain switching and phase transformation in the material, a simplified description, inspired from a full multiscale approach [48], is adopted. The material is considered as a collection of pseudo-cubic grains with orientations given by the Euler angles ($\varphi_1, \psi, \varphi_2$) [49]. Each orientation is treated itself as a collection of ferroelectric domains with six possible orientations α_T for the polarization in the case of the tetragonal variant, and twelve possible orientations α_O in the case of the orthorhombic variant. The volume fraction of domains with orientation α_T (resp. α_O) in the tetragonal (resp. orthorhombic) phase is noted f_T^α (resp. f_O^α). As a first approach, the energy balance is supposed to be driven only by the applied macroscopic

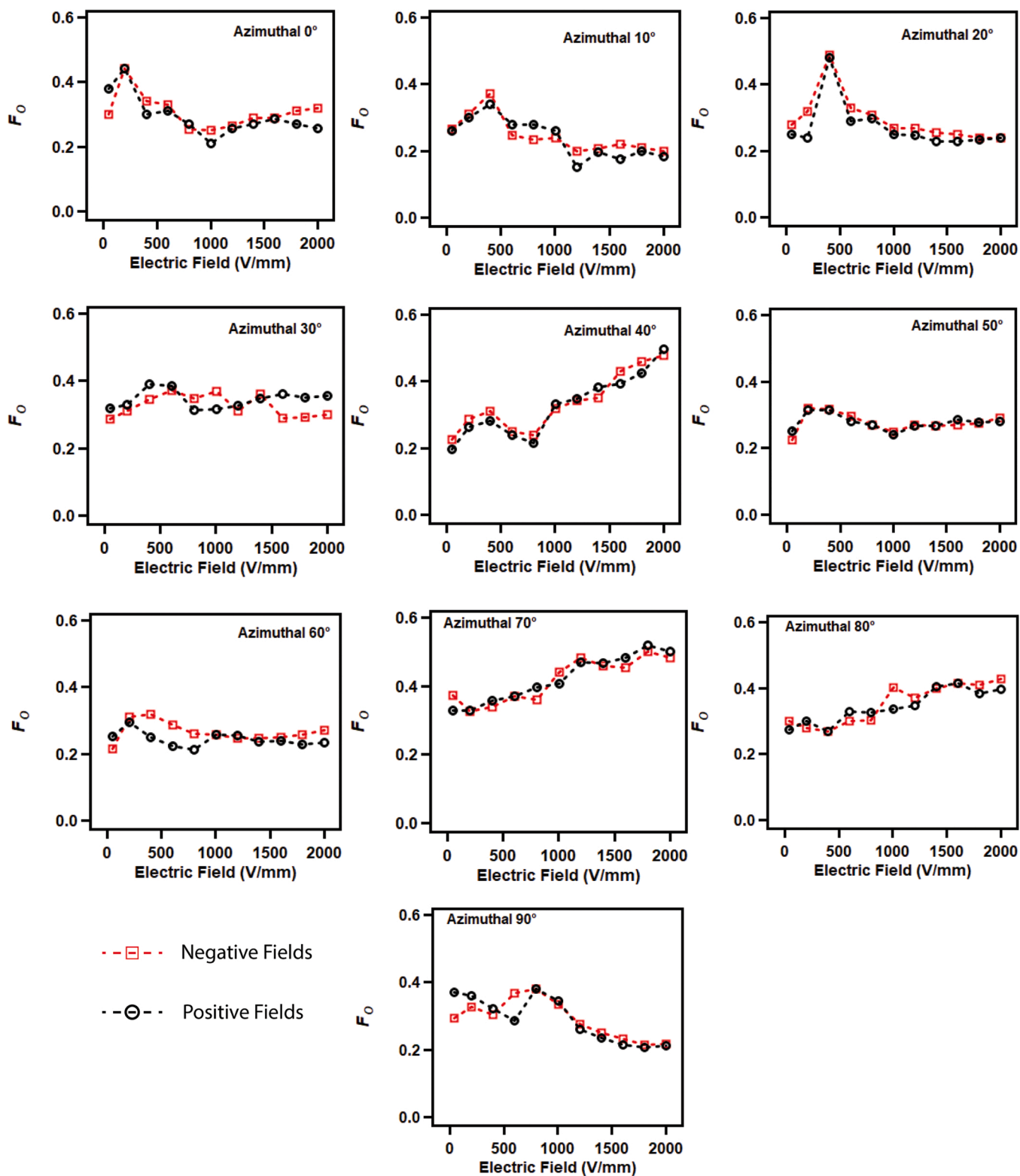


Fig. 9. Changes in the orthorhombic phase fraction, F_O , as a function of azimuthal angle with respect to the electric field direction.

electric field E (supposed to be homogeneous within the material) and its direction with respect to grain orientations. For a given grain orientation $(\varphi_1, \psi, \varphi_2)$, and for a given domain orientation α , the electrostatic energy W^α is written as a function of the spontaneous polarization P_0 of the material (4). The value of P_0 is assumed to be identical in both tetragonal and orthorhombic phases.

$$W_T^\alpha = -P_0\alpha_T.E \text{ and } W_O^\alpha = -P_0\alpha_O.E \tag{4}$$

The volume fraction of each domain orientation is then assumed to be defined according to a Boltzmann-type relation [48]:

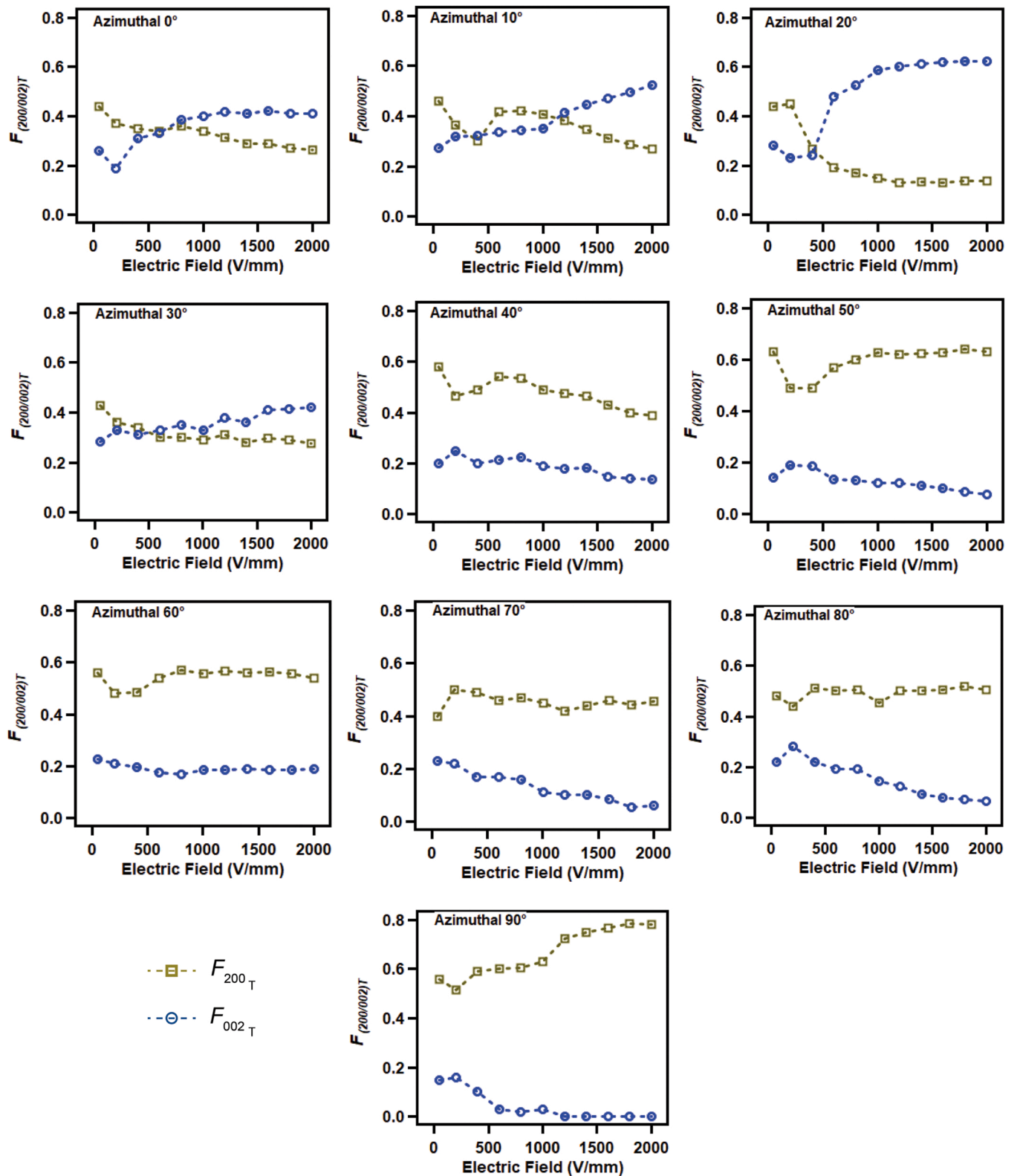


Fig. 10. Change in tetragonal phase domain variant fractions, F_{002} , and F_{200} , as functions of azimuthal angle with respect to the electric field direction for negative applied electric fields (for positive electric fields, see Fig. S2 in the SI).

$$f_T^\alpha = \frac{\exp(-A_T W_T^\alpha)}{\sum_\alpha \exp(-A_T W_T^\alpha)} \text{ and } f_O^\alpha = \frac{\exp(-A_O W_O^\alpha)}{\sum_\alpha \exp(-A_O W_O^\alpha)} \quad (5)$$

A_T (resp. A_O) is a material constant (positive), supposed to be proportional to the initial susceptibility of the material in the T (resp. O)

phase. Eq. (5) shows that the lower the electrostatic energy of a ferroelectric domain orientation, the higher its probability. On the contrary, a high electrostatic energy promotes the disappearance of the corresponding ferroelectric domain. Hence, for a given pseudo-cubic orientation, Eq. (5) allows to define, for a given variant (T or O), the relative

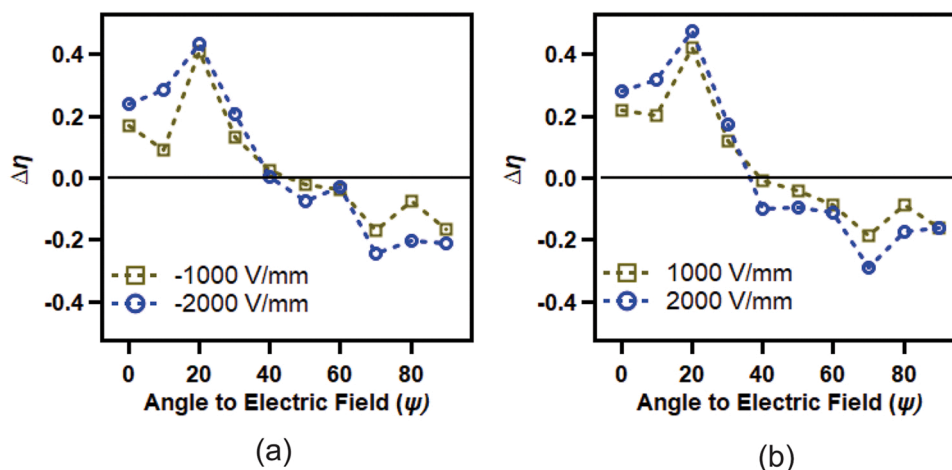


Fig. 11. Domain switching fractions, $\Delta\eta$, in the T phase as function of orientation with respect to the electric-field direction, ψ , for (a) negative, and (b) positive electric fields.

proportion of the different possible domain orientations. It therefore provides the average polarization corresponding to this specific variant in a specific orientation. The average energy of a given variant corresponding to the macroscopic field E can also be calculated:

$$W_T = \langle W_T^\alpha \rangle = \sum_{\alpha} f_T^\alpha W_T^\alpha \quad \text{and} \quad W_O = \langle W_O^\alpha \rangle = \sum_{\alpha} f_O^\alpha W_O^\alpha \quad (6)$$

These latter formulas allow to compare, for a given electric-field level E and a given pseudo-cubic orientation (ϕ_1, ψ, ϕ_2), the energy level corresponding to the tetragonal and orthorhombic variants. It can be assumed that a lower energy level will promote the appearance or stability of a variant, while a higher energy level will favor the other variant. These energy levels have been calculated for different sets of orientations as shown in Figs. 12 and 13. The material parameters used for the calculation are given in Table 1.

For a given orientation ψ (as shown in Fig. 3), various grain orientations can fulfil the Bragg condition. This is why, for each value of ψ , it is necessary to explore a range of ϕ_2 angles, resulting in various energy levels. This variety of energy levels is reflected by the error bars in Figs. 12 and 13.

Fig. 12 shows the energy levels of T and O phase variants as a function of the applied electric field for different orientations ψ . Fig. 13 shows the energy levels of T and O phase variants as a function of the orientation ψ at different levels of applied electric field. At low fields (see Fig. 13(a)), the orthorhombic is favored for all angles. However the difference between the two energy states is very small (about 2 kJ/m^3) and the phase transition would probably require some additional energy for phase boundaries to overcome pinning effect from defects or internal stresses [20],[50], so that the energy balance favors a *statu quo* and there is no significant T to O phase transition. When the electric field is further increased, the T phase becomes the favored phase for low and high angles, while the middle orientations between 30° and 60° azimuthal angle show a preference for the O phase. It should be noticed that the difference between the energy levels of the two phases can reach very high values, up to 100 kJ/m^3 at 1.2 kV/mm . For azimuthal angles lower than 30° , it seems possible that after a transition to an O phase, the material goes back to the initial T phase that is clearly favored at high field. At intermediate angles between 30° and 60° , any phase change from T to O is likely to be irreversible since the O phase is clearly favored at high field, and the contrast between the levels of energy of O and T phases keeps increasing with the electric field. The configuration is more complex for orientations with azimuthal angle higher than 60° since, depending on the orientation of the grain, either T or O phases can be favored. For some orientations, some of the T phase variants (a-domains) can decrease in volume fraction to the benefit of an increase in O

phase fraction while for other orientations some T phase variants (a-domain) can become favorable and therefore grow at the expense of O phase domains.

The energy drive for transition between T to O phases, as calculated above from the multiscale model, agrees well with the experimentally observed electric-field-induced orthorhombic phase volume fraction. Fig. 15 shows ΔF_O as a function of angle to the electric field, ψ , where $\Delta F_O = F_{O,2000} - F_{O,45}$; $F_{O,2000}$ and $F_{O,45}$ refer to the value of F_O for applied electric fields of 2000 V/mm and 45 V/mm , respectively. The values shown in Fig. 15 are average of those measured for positive and negative applied electric fields. The value of ΔF_O is negative for $\psi \leq 25^\circ$. In contrast, the value of ΔF_O is positive for $30^\circ \leq \psi \leq 80^\circ$, but is largest for $\psi \sim 40^\circ$ and smallest for $\psi \sim 60^\circ$. These observations are consistent with the relative difference between the W_{tot} curves for the T and O phases at $E = 2000 \text{ V/mm}$, as shown in Fig. 13. The first cross-over point between the W_{tot} curves for the T and O phases (see Fig. 13) is located at $\psi \sim 25^\circ$, below which it can be expected that the O phase will be less favored, and therefore we obtain a negative value for ΔF_O for these orientations. For $30^\circ \leq \psi \leq 80^\circ$, the volume fraction of the induced O phase will depend on the maximum difference between the W_{tot} curves for the T and O phases. Since this difference is largest for $\psi \sim 40^\circ$, we experimentally observe the highest value of ΔF_O for this orientation. Note that the difference between the W_{tot} curves of the two phases is lowest for $\psi \sim 60^\circ$, which is therefore reflected in the lowest value of ΔF_O for this angle. For directions orthogonal to the electric-field, $\psi \sim 90^\circ$, some domain variants of the T phase are clearly favored over those of the O phase, since they have significantly lower W_{tot} – this is reflected in a negative value for experimentally observed ΔF_O for this angle.

It should be noted that the relative positions of the curves with respect to W_{tot} in Figs. 12 and 13 will be modified by a change in the values listed in Table 1. However, for comparable values of A_T and A_O , the general conclusions drawn here with regard to orientation dependence of phase and domain switching fractions will be similar (see Figs. S3 and S4 in the SI).

5. Structure-property correlation

Fig. 3 demonstrates the attractive electromechanical properties of the Sn-doped BCZT ceramics. For cyclic electric field of maximum amplitude 2 kV/mm , a large maximum strain of $\sim 0.08\%$ is observed. Most importantly, two different regimes for the electric-field-induced strain response is evident. In the first regime, a sharp increase in electric-field-induced strain is observed below 1 kV/mm for a maximum strain value of $\sim 0.06\%$. However, further increment in electric-field-induced strain is significantly reduced in the second regime for

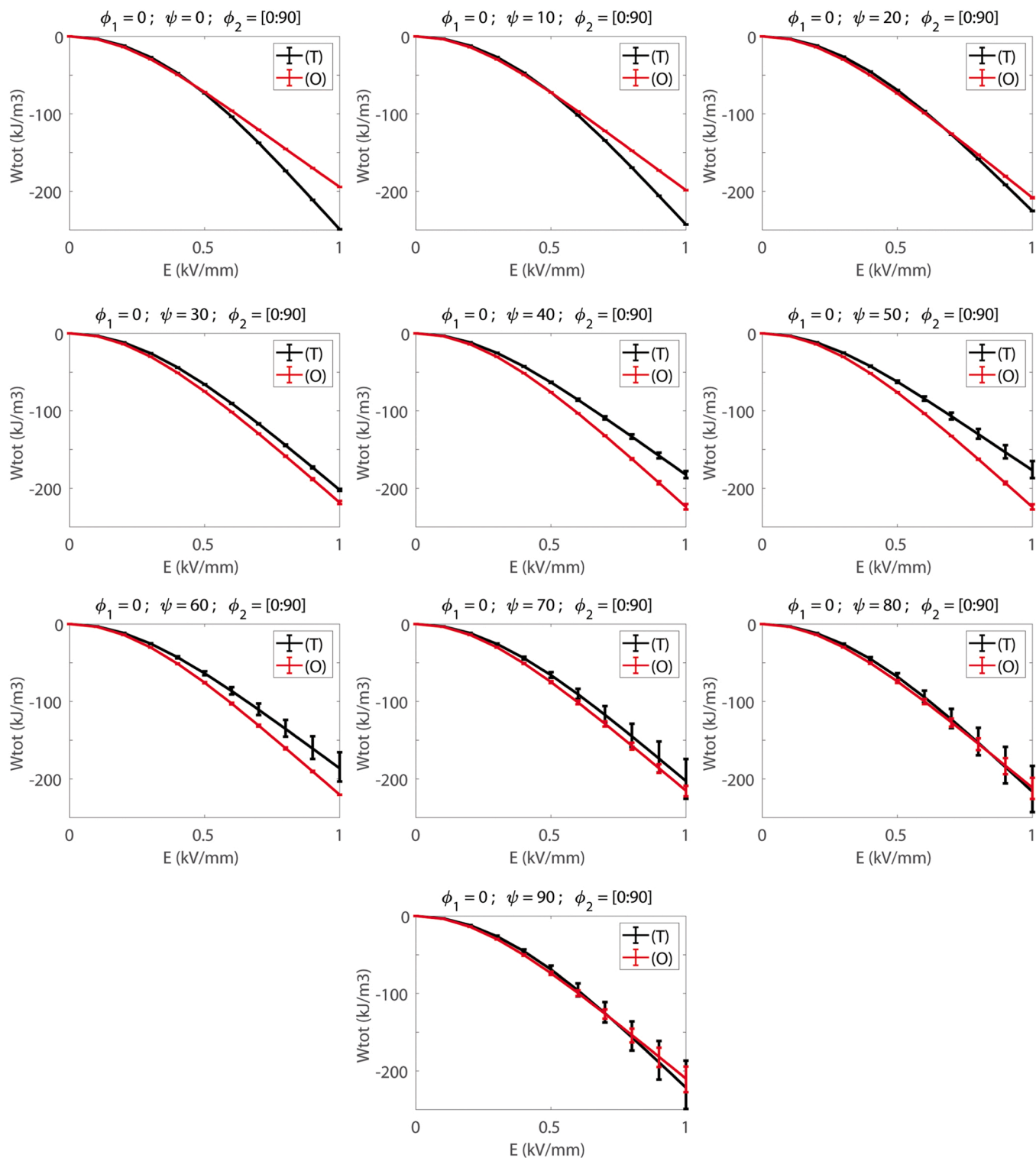


Fig. 12. Average energy of the tetragonal (*T*) and orthorhombic (*O*) phases as a function of the applied electric field for various azimuthal angles from 0° to 90°.

electric fields exceeding 1 kV/mm. As explained in our earlier work, such properties make this material particularly suitable for use in high-precision piezoelectric actuators [31]. The results presented in the current work help to clarify the micromechanisms contributing to the macroscopic electric-field-induced strain response of Sn-doped BCZT ceramics.

As shown in Fig. 11, we observe the most significant increase in $\Delta\eta$, or the 90° domain switching fraction in the *T* phase for electric fields lower than 1 kV/mm. However, with further increase in electric field to

2 kV/mm, there is only marginal increase in $\Delta\eta$. Such field-dependent domain switching behavior is corroborated by the results from micromechanical modeling, as shown in Fig. 14. The field-dependent behavior of $\Delta\eta$ correlates well to the electric-field-induced macroscopic strain response (Fig. 3). Furthermore, our results clarify that the domain switching process within the *T* phase is predominantly observed for grains with their 002_{pc} poles oriented within 20° to the electric-field direction. For these grains, the 90° domain switching process proceeds through a unique reversible *T*-to-*O*-to-*T* phase transformation

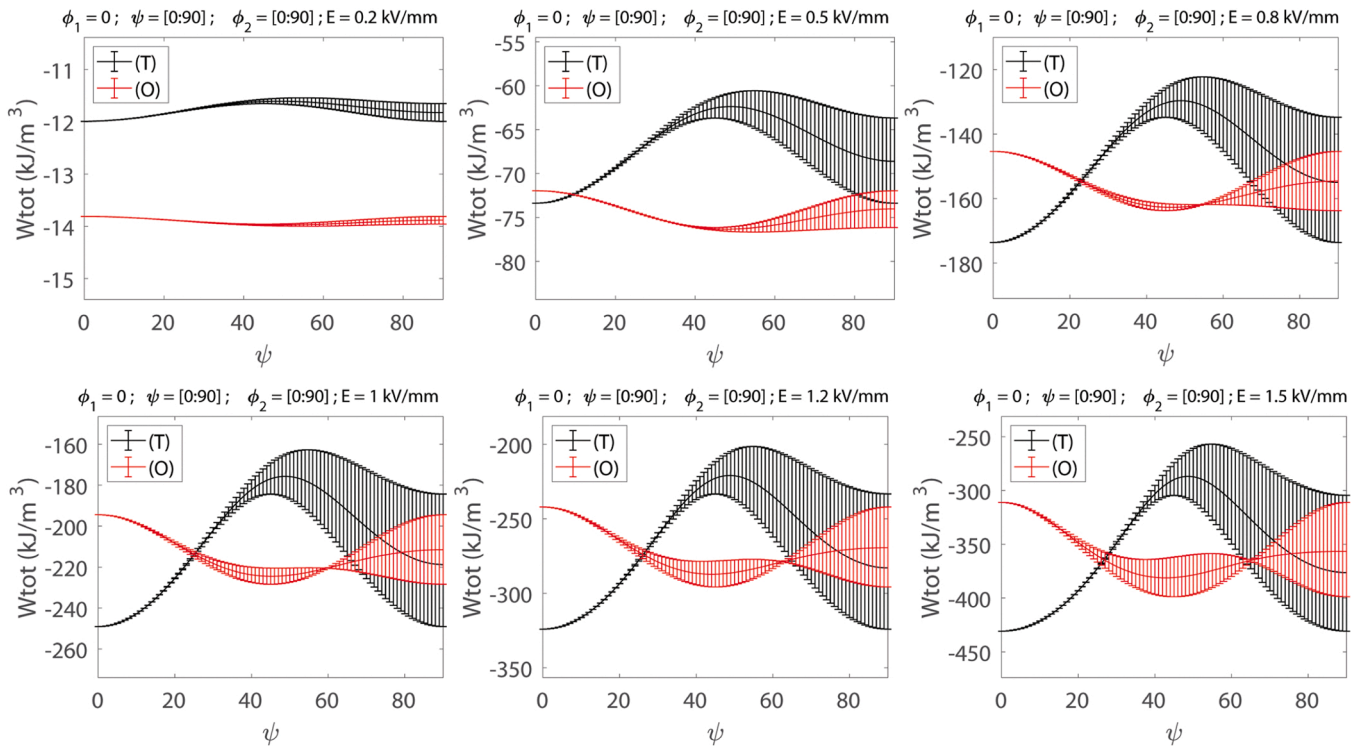


Fig. 13. Average energy of the tetragonal (*T*) and orthorhombic (*O*) phases as a function of the azimuthal angle at various electric field levels.

Table 1
Material properties used for calculations shown in Fig.s 11 and 12.

Parameter	P_0	A_T	A_O
Value	0.3	$1 \cdot 10^{-5}$	$1.2 \cdot 10^{-5}$
Unit	$C \cdot m^{-2}$	$m^3 \cdot J^{-1}$	$m^3 \cdot J^{-1}$

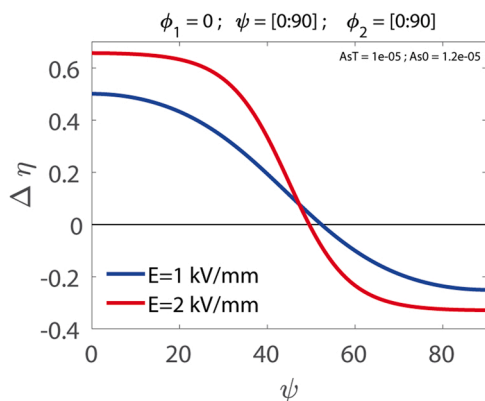


Fig. 14. Multiscale modeling prediction of the domain switching fractions, $\Delta\eta$, in the *T* phase as function of orientations with respect to the electric-field direction, ψ .

mechanism, which is exhausted when the applied electric-field magnitude reaches 1 kV/mm. Further increase in electric field to 2 kV/mm mainly causes increasing irreversible transformation from *T* to *O* phase, which is most predominant for grains with their 002_{pc} pole oriented 40° to the electric-field direction, but contributes marginally to the macroscopic strain.

Noteworthy that for angles 0°–10° the experimentally determined $\Delta\eta$ (Fig. 11) are anomalously low as compared to what is predicted from

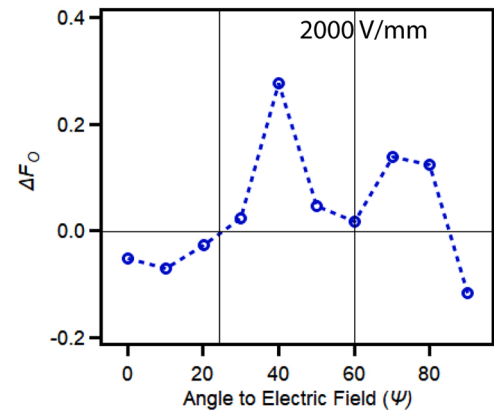


Fig. 15. Electric-field-induced orthorhombic phase fraction, ΔF_O , as a function of orientation with respect to the electric-field direction for electric-field magnitude of 2000 V/mm. See text for detailed description.

the micromechanical model (Fig. 14). This may be due to the strong interaction between the domain walls and defect dipoles in the material. During the application of initial poling field, both the polarization of the domains and the defect dipoles tend to be aligned with the electric-field direction. The domain walls and the defect dipoles may form low-energy configurations, which are then stabilized against further reorientation [47]. If the defect dipoles are strongly aligned to the initial poling direction, it is therefore possible that upon subsequent electric-field application the domain switching will be suppressed for these orientations. It is also possible that internal compressive stresses generated subsequent to poling may suppress further domain switching, and this effect is strong for orientations closely aligned to the poling electric-field direction [20].

Overall, our micromechanical model helps to clarify the phase transition behavior between the *T* and *O* phases. For materials with coexisting *O* and *T* phases, and for which the dielectric susceptibility

within the *T* and *O* phases are comparable, we discovered the unique phenomenon of a reversible *T*-to-*O*-to-*T* phase transition for grain orientations with their 001 axis within 20° of the electric-field direction. These results therefore indicate that large electrostrain conducive for precision actuators can be most effectively achieved in textured ceramics, in which the 001 axes of the grains are oriented within 20° of the electric-field direction.

6. Conclusions

We examine here the micromechanisms of electric-field-induced structural changes in a Pb-free piezoceramic with coexisting tetragonal and orthorhombic phases from *in situ* high-energy X-ray diffraction and multiscale modeling. A unique orientation-dependent phase transition phenomenon between tetragonal and orthorhombic phases is revealed for Sn-doped BCZT piezoceramics with composition near orthorhombic-tetragonal phase boundary. Specifically, we observe a reversible *T*-to-*O*-to-*T* phase transformation for grains whose 002_{pc} poles are oriented within 20° of applied electric-field direction. In contrast, a continuous increase in *O* phase fraction is observed for grains whose 002_{pc} poles are oriented 30°–80° with respect to the electric-field direction, while the relative changes depend on the specific grain orientation. The grains with their 002_{pc} poles oriented 40° to the electric-field direction exhibit a maximum volume fraction of induced *O* phase. For grains that have their 002_{pc} axes oriented orthogonal to the electric-field direction, a reverse transformation from *O* to *T* phase is observed at high electric-field magnitudes. This behavior is self-consistently explained using a micromechanical model, which predicts the nature of phase transformation phenomena based on the total energy states of the *T* and *O* phase variants as a function of grain orientation. In addition, we have evaluated the 90° domain switching ratio within the *T* phase as a function of grain orientations. In general, the results from *in situ* X-ray diffraction experiments and micromechanical modeling are self-consistent with regard to orientation-dependent domain switching behavior. However, the 90° domain switching is anomalously suppressed for grains with their 002_{pc} poles oriented within 10° to the electric-field direction, which may result from a stronger pinning of domain walls by microscopic defect dipoles for these orientations. Overall, we demonstrate a method to self-consistently describe the orientation-dependent electric-field-induced phase transition and domain switching behavior in a ferroelectric material with coexisting tetragonal and orthorhombic phases, which will be critically important for the design and application of piezoelectric ceramics in high-performance actuators.

Declaration of Competing Interest

The authors declare that they have no known competing financial interests or personal relationships that could have appeared to influence the work reported in this paper.

Acknowledgements

A.P. and S.V. gratefully acknowledge funding support from CityU (Projects No. 7005644 and 9610377). A.P. acknowledges funding support from Research Grants Council of HK (Project No. 9052026 and 9043039). L.D. and A.P. would like to acknowledge the support from the Programme Hubert Curien PROCORE (No40147VF) for partial funding, and from University Paris-Saclay in the framework of the d'Alembert fellowship program. This research used resources of the Advanced Photon Source, a U.S. Department of Energy (DOE) Office of Science User Facility operated for the DOE Office of Science by Argonne National Laboratory under Contract No. DE-AC02-06CH11357. A.P. and L.D. acknowledge technical support at APS from Richard Spencer. The assistance from Dr. José Alvarez from GeePs-CNRS for the SEM imaging of the sample is also gratefully acknowledged.

Appendix A. Supporting information

Supplementary data associated with this article can be found in the online version at doi:10.1016/j.jeurceramsoc.2023.01.051.

References

- [1] B. Jaffe, W.R. Cook, L. Jaffe, H. Piezoelectric Ceramics, Academic Press, Cambridge, 1971.
- [2] K. Uchino, Piezoelectric Actuators and Ultrasonic Motors, Kluwer Academic, Boston, 1996.
- [3] K. Uchino, Ferroelectric Devices, Marcel Dekker, 2000.
- [4] C.R. Bowen, H.A. Kim, P.M. Weaver, S. Dunn, Piezoelectric and ferroelectric materials and structures for energy harvesting applications, Energy Environ. Sci. 7 (2014) 25.
- [5] T. Mori, S. Priya, Materials for energy harvesting: at the forefront of a new wave, MRS Bull. 43 (2018) 176–180.
- [6] S. Roundy, S. Trolier-McKinstry, Materials and approaches for on-body energy harvesting, MRS Bull. 43 (2018) 206–213.
- [7] D. Lupascu, J. Rodel, Fatigue in Bulk Lead Zirconate Titanate Actuator Materials, Adv. Eng. Mater. 7 (10) (2005) 882–898.
- [8] K. Uchino, Piezoelectric actuator renaissance, Phase Transit. 88 (2015) 342–355.
- [9] X. Gao, J. Yang, J. Wu, X. Xin, Z. Li, X. Yuan, X. Shen, S. Dong, Piezoelectric actuator and motors: materials, designs, and applications, Adv. Mater. Technol. 5 (2020), 1900716.
- [10] D. Damjanovic, Stress and frequency dependence of the direct piezoelectric effect in ferroelectric ceramics, J. Appl. Phys. 82 (1997) 1788–1797.
- [11] D.A. Hall, Nonlinearity in piezoelectric ceramics, J. Mater. Sci. 36 (2001) 4575–4601.
- [12] Y. Zhang, J. Glaum, M.C. Ehmke, J.E. Blendell, K.J. Bowman, M.J. Hoffman, high bipolar fatigue resistance of BCZT lead-free piezoelectric ceramics, J. Am. Ceram. Soc. 99 (2016) 174–182.
- [13] A.M. Manjon-Sanz, M.R. Dolgos, Applications of piezoelectrics: old and new, Chem. Mater. 30 (2018) 8718–8726.
- [14] A.J. Bell, O. Deubzer, Lead-free piezoelectrics—The environmental and regulatory issues, MRS Bull. 43 (2018) 581–587.
- [15] J. Rodel, J.-F. Li, Lead-free piezoceramics: Status and perspectives, MRS Bull. 43 (2018) 576–580.
- [16] J. Koruza, A.J. Bell, T. Fromling, K.G. Webber, K. Wang, J. Rodel, Requirements for the transfer of lead-free piezoceramics into application, J. Mater. 4 (2018) 13–26.
- [17] M. Liu, K.J. Hsia, M.R. Sardela Jr., *In situ* X-ray diffraction study of electric-field-induced domain switching and phase transition in PZT-5H, J. Am. Ceram. Soc. 88 (2005) 210–215.
- [18] D.A. Hall, A. Steuwer, B. Cherdhirunkorn, T. Mori, P.J. Withers, A high energy synchrotron x-ray study of crystallographic texture and lattice strain in soft lead zirconate titanate ceramics, J. Appl. Phys. 96 (2004) 4245–4252.
- [19] A. Pramanick, D. Damjanovic, J.E. Daniels, J.C. Nino, J.L. Jones, J. Am. Ceram. Soc. 94, “Origins of electro-mechanical coupling in polycrystalline ferroelectrics during subcoercive electrical loading”, 293–309 (2011).
- [20] L. Daniel, D.A. Hall, J. Koruza, K.G. Webber, A. King, P.J. Withers, Revisiting the blocking force test on ferroelectric ceramics using high energy x-ray diffraction, J. Appl. Phys. 117 (2015), 174104.
- [21] J. Zhao, S.D. Funni, E.R. Molina, E.C. Dickey, J.L. Jones, Orientation-dependent, field-induced phase transitions in soft lead zirconate titanate piezoceramics, J. Eur. Ceram. Soc. 41 (2021) 3357–3362.
- [22] W. Liu, X. Ren, Large piezoelectric effect in Pb-free ceramics, Phys. Rev. Lett. 103 (2009), 257602.
- [23] D.S. Keeble, F. Benabdallah, P.A. Thomas, M. Maglione, J. Kreisel, Revised structural phase diagram of Ba(Zr_{0.2}Ti_{0.8})O₃-(Ba_{0.7}Ca_{0.3})TiO₃, Appl. Phys. Lett. 102 (2013), 092903.
- [24] C. Ma, H. Guo, S.P. Beckman, X. Tan, Creation and destruction of morphotropic phase boundaries through electrical poling: a case study of lead-free (Bi_{1/2}Na_{1/2})TiO₃-BaTiO₃ piezoelectrics, Phys. Rev. Lett. 109 (2012), 107602.
- [25] Y. Saito, H. Takao, T. Tani, T. Nonoyama, K. Takatori, T. Homma, T. Nagaya, M. Nakamura, Lead-free piezoceramics, Science 332 (2004) 84–87.
- [26] K. Xu, J. Li, X. Lv, J. Wu, X. Zhang, D. Xiao, J. Zhu, “Superior piezoelectric properties in Potassium-sodium niobate lead-free ceramics”, Adv. Mater. 28 (2016) 8519–8523.
- [27] W. Jo, J.E. Daniels, J.L. Jones, X. Tan, P.A. Thomas, D. Damjanovic, J. Rodel, Evolving morphotropic phase boundary in lead-free (Bi_{1/2}Na_{1/2})TiO₃-BaTiO₃ piezoceramics, J. Appl. Phys. 109 (2011), 014110.
- [28] T. Iamsari, G. Tutuncu, C. Uthaisar, S. Wongsanmai, S. Pojprapai, J.L. Jones, Electric field-induced phase transitions in Li-modified Na_{0.5}K_{0.5}NbO₃ at the polymorphic phase boundary, J. Appl. Phys. 117 (2015), 024101.
- [29] H. Guo, B.K. Voas, S. Zhang, C. Zhou, X. Ren, S.P. Beckman, X. Tan, Polarization alignment, phase transition, and piezoelectricity development in polycrystalline 0.5Ba(Zr_{0.2}Ti_{0.8})O₃-0.5(Ba_{0.7}Ca_{0.3})TiO₃, Phys. Rev. B 90 (2014), 014103.
- [30] B. Zhang, J. Wu, X. Cheng, X. Wang, D. Xiao, J. Zhu, X. Wang, X. Lou, Lead-free piezoelectrics based on potassium-sodium niobate with giant d₃₃, ACS Appl. Mater. Inter. 5 (2013) 7718–7725.
- [31] S. Venkateswarlu, K.K. Venkataraman, V. Segouin, F.P. Marlton, H.C. Hin, D. Chernyshov, Y. Ren, M.R.V. Jorgensen, S. nayak, J. Rodel, L. Daniel, A. Pramanick, Large electromechanical strain and unconventional domain

- switching near phase convergence in a Pb-free ferroelectric, *Comm. Phys.* 3 (2020) 193.
- [32] H.M. Rietveld, A Profile Refinement Method for Nuclear and Magnetic Structures, *J. Appl. Crystallogr.* 2 (1969) 65–71.
- [33] M. Hinterstein, J. Rouquette, J. Haines, Ph Papet, M. Knapp, J. Glaum, H. Fuess, Structural description of the macroscopic piezo- and ferroelectric properties of lead zirconate titanate, in: *Phys. Rev. Lett.*, 107, 2011.
- [34] L. Fan, J. Chen, Y. Ren, X. Xing, Structural correlation to piezoelectric and ferroelectric mechanisms in rhombohedral $\text{Pb}(\text{Zr,Ti})\text{O}_3$ ceramics by in-situ synchrotron diffraction, *Inorg. Chem.* 57 (2018) 3002–3007.
- [35] G. Esteves, C.M. Fancher, S. Rohrig, G.A. Maier, J.L. Jones, M. Deluca, *Acta Mater.* 132 (2017) 96–105.
- [36] N.C. Popa, D. Balzar, Elastic strain and stress determination by Rietveld refinement: generalized treatment for textured polycrystals for all Laue classes, *J. Appl. Cryst.* 34 (2001) 187–195.
- [37] J. Chen, J.E. Daniels, J. Jian, Z. Cheng, J. Cheng, J. Wang, Q. Gu, S. Zhang, origin of large electric-field-induced strain in pseudo-cubic BiFeO_3 - BaTiO_3 ceramics, *Acta Mater.* 197 (2020) 1–9.
- [38] M. Hinterstein, M. Hoelzel, J. Rouquette, J. Haines, J. Glaum, H. Kungl, M. Hoffman, Interplay of strain mechanisms in morphotropic piezoceramics, *Acta Mater.* 94 (2015) 319–327.
- [39] J. Hao, W. Bai, W. Li, J. Zhai, Correlation between the microstructure and electrical properties in high-performance $(\text{Ba}_{0.85}\text{Ca}_{0.15})(\text{Zr}_{0.1}\text{Ti}_{0.9})\text{O}_3$ lead-free piezoelectric ceramics, *J. Am. Ceram. Soc.* 95 (2012) 1998–2006.
- [40] Z. Tomicevc, F. Hild, S. Roux, Mechanics-aided digital image correlation, *J. Strain Anal. Eng. Des.* 48 (2013) 330–343.
- [41] M.H. Malakooti, H.A. Sodano, Noncontact and simultaneous measurement of the d_{33} and d_{31} piezoelectric strain coefficients, *Appl. Phys. Lett.* 102 (2013), 061901.
- [42] D. Chen, E. Carter, M. Kamlah, Deformation behavior of lead zirconate titanate ceramics under uniaxial compression measured by the digital image correlation method, *Smart Mater. Struct.* 25 (2016), 097001.
- [43] V. Segouin, M. Domenjoud, Y. Bernard, L. Daniel, Development of a 2D DIC experimental tool for piezoelectric strains measurements. *International Digital Imaging Correlation Society*, Springer International Publishing, 2017, pp. 45–50.
- [44] V. Segouin, M. Domenjoud, Y. Bernard, L. Daniel, Mechanics-aided digital image correlation for the investigation of piezoelectric and ferroelectric behaviour of a soft PZT, *J. Eur. Ceram. Soc.* 39 (2019) 2091–2102.
- [45] V. Segouin, M. Domenjoud, Y. Bernard, L. Daniel, Electro-mechanical behavior of ferroelectrics: insights into local contributions from macroscopic measurements, *Acta Mater.* 211 (2021), 116870.
- [46] J.E. Daniels, J.L. Jones, T.R. Finlayson, Characterization of domain structures from diffraction profiles in tetragonal ferroelastic ceramics, *J. Phys. D: Appl. Phys.* 39 (2006) 5294.
- [47] M.C. Ehmke, N.H. Khansur, J.E. Daniels, J.E. Blendell, K.J. Bowman, *Acta Mater.* 66 (2014) 340–348.
- [48] L. Daniel, D. Hall, P.J. Withers, A multiscale model for reversible ferroelectric behaviour of polycrystalline ceramics, *Mech. Mater.* 71 (2014) 85–100.
- [49] U.F. Kocks, C.N. Tomé, H.-R. Wenk, *Texture and Anisotropy: Preferred orientations in polycrystals and their effect on material properties*, Cambridge University Press, 1998, pp. 44–94.
- [50] A. Pramanick, A.D. Prewitt, J.S. Forrester, J.L. Jones, Domains, domain walls and defects in perovskite ferroelectric oxides: a review of present understanding and recent contributions, *Crit. Rev. Solid State Mater. Sci.* 37 (2012) 243–275.